Simulation of Ice Shedding From Rotating Parts Using Phase-Field Fracture and Cohesive Zone Models

Dorian Nezzar, Johann Rannou, Philippe Villedieu, Lokman Bennani, Morgan Balland, Clément Vénuat

Simulation of ice shedding from rotating parts using phase-field fracture and cohesive zone models

D. Nezzar* and J. Rannou†
ONERA/DMAS, Université Paris-Saclay, F-92322 Châtillon, France

P. Villedieu‡ and L. Bennani§
ONERA/DMPE - Université de Toulouse, F-31055 Toulouse, France

M. Balland¶ and C. Venuat‖
Safran Aircraft Engines, F-77550, Moissy-Cramayel, France

The aim of this work is to develop a numerical methodology for the simulation of ice shedding from rotating parts in an aircraft engine. The goal is to estimate the size of the detached ice blocks and to assess the feasibility of such simulations for 3D industrial cases. This work relies on mechanical properties available from recent collaborative projects on the characterization of adhesive and cohesive properties of accreted ice of different substrates. The simulations are performed with the finite element software *Z-set* using a *phase-field fracture* model coupled to a *cohesive zone model* to capture cracks in the ice volume, at the ice/substrate interface or in mixed modes.

I. Nomenclature

$\boldsymbol{\varepsilon}$	=	second order linear elastic strain tensor, MPa
ϵ	=	stopping criterion of the staggered scheme
E	=	Young's modulus, MPa
$\mathbb{E}$	=	fourth order linear elastic strain tensor, MPa
G_c	=	Griffith critical energy release rate, $\mathrm{mJ/mm^2}$
i	=	iteration index of the staggered scheme
l_c	=	internal length of the phase-field model, mm
n	=	time step index of the Newton-Raphson algorithm iteration
n_0	=	freezing fraction parameter
$\boldsymbol{\sigma}$	=	second order Cauchy stress tensor, MPa
σ_{rr}	=	radial component of the stress tensor $\boldsymbol{\sigma}$, MPa
σ_{rz}	=	shear component of the stress tensor $\boldsymbol{\sigma}$, MPa
ϕ	=	phase-field variable
$\nabla\phi$	=	gradient vector of the phase-field variable, $\mathrm{mm^{-1}}$
Ψ_0	=	strain energy density, $\mathrm{J/m^3}$
$\mathbf{u}$	=	displacement vector, mm
t	=	simulation time, s
$\langle \boldsymbol{A} \rangle^+$	=	denotes the positive part of a second order $\boldsymbol{A}$ define as $\sum_j \langle A_j \rangle n_j \otimes n_j$ with A_j the eigenvalues and n_j the eigenvectors
$\langle x \rangle$	=	denotes the positive part of a scalar x define as $\langle x \rangle = \max(0, x)$
$^{\mathrm{bulk}}$	=	superscript related to bulk (ice) properties
$^{\mathrm{int}}$	=	superscript to interface properties
$_c$	=	subscript to indicate critical values

*PhD Candidate, ONERA/DMAS, dorian.nezzar@onera.fr
†Research scientist - PhD, ONERA/DMAS, johann.rannou@onera.fr
‡Senior scientist - PhD, ONERA/DMPE
§Research scientist - PhD, ONERA/DMPE
¶Head of Inclement weather team, Safran Aircraft Engines
‖Aerothermal Engineer, Safran Aircraft Engines

II. Introduction

Icing in aeronautics is considered as one of the most critical phenomena for an aircraft engine. Ice formation is caused by supercooled water droplets, which will freeze at impact on certain surfaces exposed to the airflow. In the case of an engine, ice can accrete on its rotating components and shed due to centrifugal forces. This can lead to damage the engine as detached ice can impact other components of the turbomachine or create vibrating phenomena resulting from an unbalanced weight distribution caused by the residual ice. However, during icing tests on rotating components, access to informations on ice shedding mechanisms remains limited due to high rotation speeds and instrumentation difficulties. Therefore, numerical simulation appears to be a promising solution to study ice shedding. Ice shedding can occur following several modes of failures: adhesive failure at the interface between ice and substrate, cohesive failure within ice bulk or following a mixed mode (Fig. 1). Therefore, in this paper the numerical approach is based on a combination between a *phase-field fracture* model [1, 2] in the bulk and a *cohesive zone model* [3, 4] at the interface. Phase-field fracture models have already been used in the context of electrothermal de-icing systems in [5, 6] and electromechanical resonant de-icing system in [7].

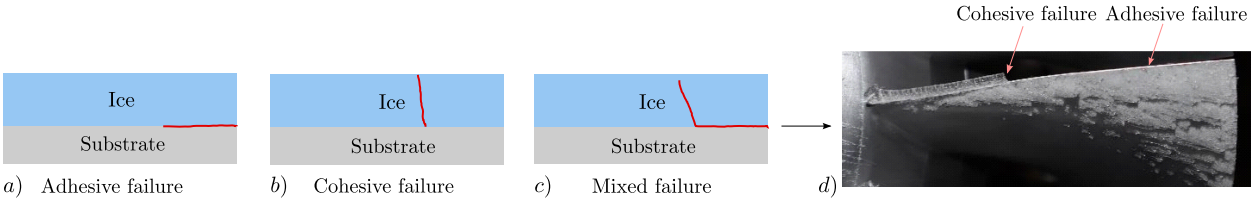

Fig. 1 Different type of ice failure on rotating substrate (left), example of mixed failure observed during icing test on rotating blades in the ICE GENESIS project [8] (right)

In section III, we briefly introduce the basic concepts of the phase-field fracture model (closely related to gradient-based damage model [9]) as a variational approach of the classical Griffith theory for brittle fracture [10]. We also present the coupled equations of the mechanical equilibrium problem and the fracture problem, with details on their numerical resolution using an staggered scheme as introduced for phase-field fracture problems in [2]. Despite quasi-static loading, fracture problems can induce dynamic instabilities in the structural response, characterized by abrupt force-displacement changes during rapid crack propagation, known as *snap-back* or *snap-through* instabilities. The associtated excess of energy is converted into kinetic energy and then cause numerical convergence difficulties with a quasi-static resolution [11]. Hence, to address these instabilities, an implicit dynamic solver is employed with adaptive time stepping, to restore stability and regularity of the solution thanks to inertia effect. Since the computation time can increase drastically, a parallelization method by domain decomposition is used with a staggered scheme resolution as in [11].

In section IV, we highlight the importance of certains ice mechanical properties with regard to the phase-field fracture model selected from the existing ones: AT1, AT2 and others listed in [12]. Indeed, their relation with the length scale parameter l_c depending on the phase-field model chosen, allows to link the initiation and propagation of a crack respectively to a value of a critical stress σ_c^{pf}[MPa] and to the critical energy release rate G_c^{pf}[mJ/mm^2] using Eq. 10.

In section V, the case of a 3D ice block accreted on a rotating substrate is studied to assess the numerical methodology. This configuration is shown in Fig. 2 and is inspired from the centrifugal adhesion test in [13]. The numerical model is completed with 1D analytical formulas of the stress fields in the ice and at its interface in order to identify the location of the crack initiation and the potential location of a crack bifurcation between the volume and the interface, as observed experimentally (photo Fig. 1d). Finaly, we show the influence of the material parameters on the solution of the fracture problem, at the interface and in the volume, through simulation results for three differents interface properties.

III. Fracture model

During ice shedding, cracks may nucleate and propagate within the ice bulk or at the ice/substrate interface. The crack then possibly propagates in a mixed regime, branching from the bulk to the interface or from the interface to the bulk (Fig. 1c).

In this work, we use concepts of quasi-brittle fracture mechanics which basically involves two sets of parameters related to two classes of criteria. A stress criterion typically accounts for the crack nucleation while a surface energy criterion like the Griffith one accounts for the crack propagation. We have decided here to model the bulk and the interface cracks by the mean of two different models : phase-field fracture model for the bulk and cohesive zone models

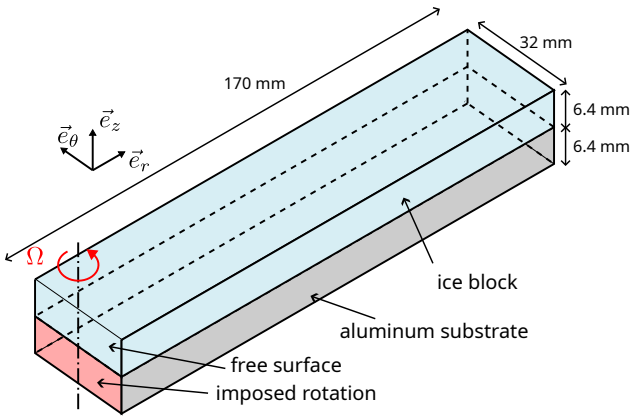

Fig. 2 Mechanical model with simplified geometry of ice accreted on a rotating substrate

for the interface. The first reason for this is that the fracture sets of parameters for the bulk and for the interface are a priori independent. The interface mechanical properties depend on the ice properties but also from the substrate itself (material, roughness, etc). In this respect, starting from section IV, superscripts $^{\text{bulk}}$ and $^{\text{int}}$ will be used to distinguish the materials parameters that are related to the bulk and to the interface respectively. The second reason is that cohesive zone models are dedicated to model interfaces in a very efficient way. Section III.B will show that this kind of models naturally include both stress and toughness criteria. Their numerical implementation through interface finite elements that are inserted within the initial mesh makes them efficient when the crack surface is a priori known. However in the bulk the crack path is however not known a priori and one has to use an other kind of model. To this extend phase-field fracture mechanics models are suitable. Whereas beeing expensive they can deal with both nucleation and propagation of cracks in a bulk described is section III.A.

A. Phase-field fracture model

Phase-field fracture model, also known as the variational approach to brittle, fracture has been introduced in [1, 2] and later popularized by [14]. It was initially thought as a new way to handle the Griffith's linear elastic fracture mechanics theory[10] (LEFM) of brittle materials which describes the crack propagation (not nucleation) in elastic media. The Griffith theory consists in minimizing the following functional with respect to the displacement field u and the unknown cracked surface Γ :

$$\mathcal{E}(u,\Gamma) = \underbrace{\int_{\Omega/\,\Gamma} \psi_0\left(\boldsymbol{\varepsilon}\left(u\right)\right) dV}_{\Psi_e} + \underbrace{G_c \int_{\Gamma} dS}_{\Psi_c} - \mathcal{P} \tag{1}$$

where Ψ_e is the elastic strain energy of the whole domain Ω, $\psi_0 = \frac{1}{2}\boldsymbol{\varepsilon}(u) : \mathbb{E} : \boldsymbol{\varepsilon}(u)$ being the elastic energy density computed from the infinitesimal strain tensor $\boldsymbol{\varepsilon}(u)$ and the elastic Hooke operator $\mathbb{E}$. Ψ_c is the energy dissipated during the cracking process and $\mathcal{P}$ is the work of the prescribed external forces. In the Griffith's theory the critical energy release rate G_c is supposed to be a material property that characterizes the resistance of a material to crack propagation. Since Γ appears as the integration domain in Ψ_c, it is not possible to handle it numerically. To circumvent this difficulty, it has then been proposed in [2] to approximate Ψ_c by the following expression :

$$\Psi_c \approx G_c \int_\Omega \frac{1}{2}\left(\frac{1}{l_c}\phi^2 + l_c(\nabla\phi)^2\right) dV \tag{2}$$

The unknown of the functional is no more the geometry of the crack Γ but is a volume field ϕ (the so-called phase-field) that can be discretized in a finite element framework. The model is built so that a value of $\phi = 0$ stands for a pristine material while a value of $\phi \in]0, 1]$ stands for a degraded material following this relation :

$$\boldsymbol{\sigma} = (1-\phi)^2\,\mathbb{E} : \boldsymbol{\varepsilon} \tag{3}$$

It is worth noting that a length parameter l_c has been introduced. It has been proven in [2] that when $l_c \to 0$, the whole formulation tends to the initial Griffith's theory (Eq. 1). The phase-field principle is schematized in Fig. 3 where it can be seen that the crack is approximated by a thin band of degraded material whose thickness is characterized by l_c.

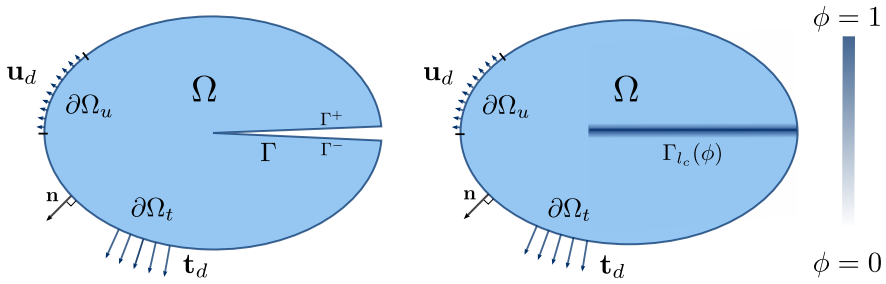

Fig. 3 Representation of a discontinuous crack surface Γ (left) with a continuous damage field Γ_{l_c} (right)

Alternatives to expression (Eq. 2) exist but the current model, also known as the AT2 model, is the simplest one from a numerical points of view since it is the only one leading to a linear phase-field equation (see Eq. 5a).

Handling expressions (1) and (2) through variational calculus leads to the following strong form of the whole model:

$$\begin{cases} \operatorname{div}\boldsymbol{\sigma} + \mathbf{f} = \rho\ddot{\mathbf{u}} & & \text{(4a)} \\ \boldsymbol{\sigma}\cdot\mathbf{n} = \mathbf{t}_d & \text{on } \partial\Omega_t & \text{(4b)} \\ \mathbf{u} = \mathbf{u}_d & \text{on } \partial\Omega_u & \text{(4c)} \end{cases}$$

and:

$$\begin{cases} \dfrac{G_c^{\text{pf}}}{2}\left[\dfrac{1}{l_c}\phi - l_c\Delta\phi\right] = (1-\phi)\mathcal{H}\left(\Psi_0{}^+\right) & & \text{(5a)} \\ \nabla\phi\cdot\mathbf{n} = 0 & \text{on } \partial\Omega & \text{(5b)} \end{cases}$$

The set of equations (4) constitutes the equilibrium problem and the set of equations (5) constitutes the phase-field problem. Equations (4b), (4c) and (5b) are the boundary conditions where $\mathbf{n}$ is the outward normal of the domain. It is worth noting that inertia forces density $\rho\ddot{u}$ (where ρ is the material density and $\ddot{u}$ is the acceleration) have been introduced in the right hand side of equation (4a), it is not straightforward from (1) and (2) but the reader should refer to [15] for further insights. Introducing inertia forces will have the advantage to simplify the handling of crack instabilities (sudden propagation of cracks in a dynamic regime) which is typical of ice shedding on rotating configurations.

It must be noted that these two sets of equations are strongly coupled through the degraded elastic relationship (3) and the source term of the phase-field equation that reads:

$$\Psi_0{}^+ = \frac{1}{2}\langle\boldsymbol{\varepsilon}(\mathbf{u})\rangle^+ : \mathbb{E} : \langle\boldsymbol{\varepsilon}(\mathbf{u})\rangle^+ \tag{6}$$

The expression $\langle\boldsymbol{\varepsilon}(\mathbf{u})\rangle^+$ means that only positive principal components of the strain tensor are considered as initially proposed in [14] to account for the fact that crack is more likely to occur under traction that under compression. The function $\mathcal{H}$ also introduced in [14] is called the history fonction. Its role is to ensure the irreversibility of the crack (cracks cannot heal themselves). If we consider the evolution of Ψ_0^+ with time, $\mathcal{H}\left(\Psi_0^+\right)$ reads at current time t:

$$\mathcal{H}\left(\Psi_0^+\right) = \max_{\tau\in[0,t]}\left(\Psi_0^+(\tau)\right) \tag{7}$$

Introducing a stress criteria for crack nucleation

As mentioned previously, phase-field fracture models tend to the Griffith theory when the internal parameter l_c tends to 0. In such a situation the stress field tends to be singular at the crack tip (providing the finite elements size is consistent with l_c). This is consistent with the brittle fracture theory which provides a surface energy propagation

criteria, but letting $l_c \to 0$ does not allow to predict crack nucleation. However, relaxing this requirement on l_c has proven to be an efficient way to switch from brittle to quasi-brittle fracture (see [16]). Indeed, if l_c has a finite value, the maximum stress is no more singular and can be controlled to fit to some kind of stress criteria that governs crack nucleation. It is common to quantify the maximum stress by considering an unidimensional homogeneous traction. Equation (5a) then reads:

$$\frac{G_c}{2l_c}\phi = (1-\phi)\frac{1}{2}E\varepsilon^2 \tag{8}$$

where E is the young modulus of the material and ε, which governs the loading, is the normal strain in the traction direction. Using the solution in ϕ of equation (8) into (3) leads to the expression of the stress in the traction direction:

$$\sigma = \left(1 - \frac{E\varepsilon^2}{\frac{G_c^{\text{pf}}}{l_c} + E\varepsilon^2}\right)^2 E\varepsilon \tag{9}$$

The stress–strain responses for different internal length l_c are plotted in Fig. 4. It is clear that the response exhibits a maximum stress called σ_c and derivation of expression (9) gives :

$$\sigma_c^{\text{pf}} = \frac{9}{16}\sqrt{\frac{EG_c^{\text{pf}}}{3l_c}} \tag{10}$$

In practice, in order to control the admissible maximum stress in the bulk of ice, l_c will be chosen such as to respect relation (10). For a comprehensive description of fracture phase-field models, the reader is referred to [12].

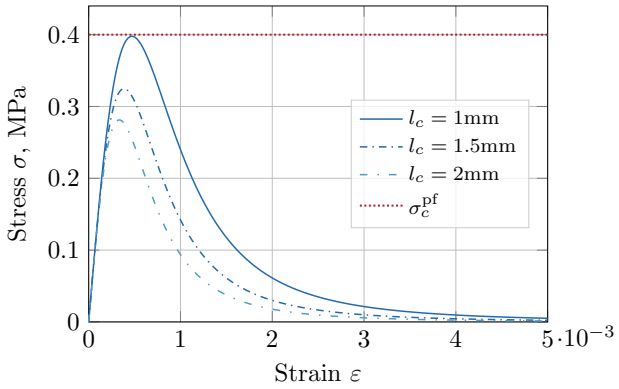

Fig. 4 Representation of the 1D homogeneous traction stress-strain response of the AT2 phase-field model ($E = 1500$MPa, $G_c = 0.001$mJ/mm^2).

B. Cohesive zone model

Cohesive zone models are dedicated to model the behavior of a damageable interface. In the context of finite elements simulations, they are widely used to model debonding of a large panel of interface, and especially composite material delamination (see for instance [17]).

They basically consist in describing a non-linear relation between a "cohesive surface force" $\vec{f}$ at both sides of an interface and the opening displacement $[\vec{u}]$ as illustrated in Fig. 5a. For a pristine interface, the relation between the stress and the opening displacement is linear (related by the elastic interface stiffness K) (see Fig. 5b). When the stress reaches a maximum stress σ_c, the interface starts to degrade and the stress–opening displacement relation is $(1-\lambda)K$ where λ is a damageable variable whose role is similar to the one of ϕ for phase-field fracture. When $\lambda = 1$ the interface in completely degraded and stress can no more be transfered (except for compression). There exist a lot of variants to describe the kinetics of $\lambda(\boldsymbol{\varepsilon})$, the one selected in this work corresponds to a linear softening as depicted in Fig. 5.b. Ideally K should tend to infinity but for numerical stability reasons K is kept finite and is as high possible (see [18]). It is worth noting that the area under the stress–displacement curve corresponds to a dissipated surface energy that can be directly related to the Griffith critical energy relase rate G_c. This formulation also naturally handles the concept of

maximum stress σ_c. Cohesive zone models are therefore a very straightforward way to model both nucleation and propagation of cracks along interfaces.

The local law depicted in Fig. 5.b is inserted at each integration points of dedicated interface finite elements as depicted in dark gray in Fig. 5.c. Nodes are duplicated at each side of the interface, the geometrical gap can be null. The opening displacement at each integration point is interpolated from the displacement gap at each finite element nodes.

The transition area from a pristine interface ($\lambda = 0$) and a totally damaged one ($\lambda = 1$) is called the "process zone" (depicted in Fig. 5.a). Its characteristic size depends on the material properties (G_c and σ_c) as well as on the surrounding bulk stiffness. This length is a priori not known but it is important to make sure that the stress gradient in the process zone is properly described by the finite element discretization.

Cohesive zone model can also model the three fracture modes : mode I (opening mode), mode II/III (shear mode). $[\vec{u}]$ and $\vec{f}$ are indeed vectors. The local law depicted in Fig. 5 could actually either relate σ_{zz} to $[u_z]$ of σ_{rz} to $[u_r]$ or a more complex combination of each components and G_c and σ_c could then depend on these modes as described in [19]. In this work however, for sake of simplicity and because there is currently a lack of experimental data on the different fracture modes, mode I and modes II/III behave exactly the same way.

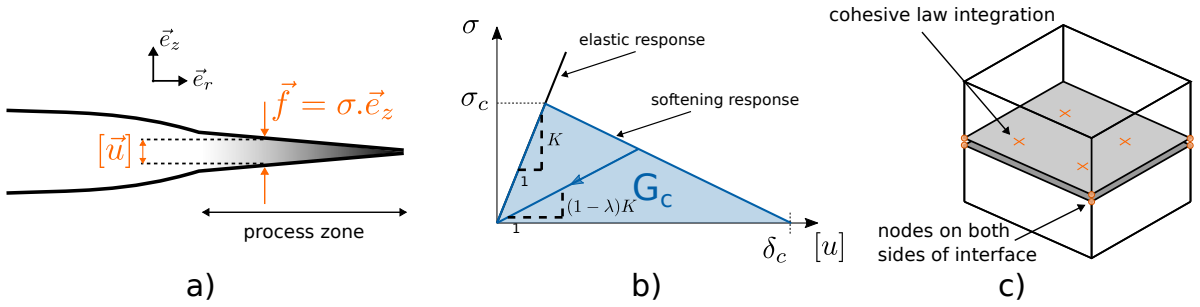

Fig. 5 Cohesive zone model : principle (a), local non-linear law (b) and interface element (gray) inserted between two volume elements (c).

C. Numerical resolution

The solution of the coupled problem (4) and (5) is performed through a staggered algorithm as initially proposed in [2]. Fig. 6 depicts the general principle: at each loading increment, from time t_n to t_{n+1}, the displacement problem (4) and the phase-field one (5) are alternately solved. At each displacement solution step the phase-field ϕ is fixed while the source term Ψ_0^+ is fixed at each phase-field step. We use two instances of the finite element solver Z-set [20] jointly developed at the École des Mines de Paris and at ONERA. The coupling is technically performed through the Python interface to the finite element code and by exchanging the fields (ϕ and Ψ_0^+) through the MPI protocol.

It must be noted that because of the cohesive zone model, the displacement problem is itself non-linear. At each displacement solution step we then benefit from the Z-set inner Newton-Raphson non-linear solver which performs its own convergence iterations. The whole loading step is then stopped when a stagnation criterion for ϕ is reached: $\|\phi^{i+1} - \phi^i\|_\infty < \epsilon$. In this paper, ϵ is set to $\epsilon = 10^{-2}$. The inertia term in the right hand side of equation 4a requires to be handled in a dynamics formulation which is achieved through the α-method implemented in Z-set.

The detailed implementation of the whole algorithm, including highly parallel framework and the time refinement heuristics is described in [11].

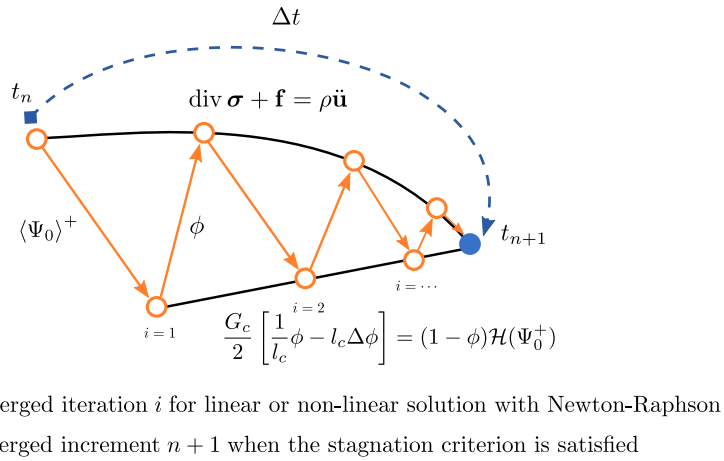

Fig. 6 Schematic of the staggered resolution for one load increment from time t_n to t_{n+1}

IV. Ice mechanical properties

In this section, we present a summary of the mechanical properties derived from recent collaborative projects, emphasizing the data obtained from icing tunnel facility experiments on accreted ice. For confidentiality reasons projects are referenced as *Study n°1* and *Study n°2* and the studied substrates are not mentioned. The purpose of this section is twofold: firstly, to demonstrate the existence of experimental tests capable of providing the material parameters required for the numerical models used in this study, and secondly, to highlight significant variability in these data due to their dependence on numerous other parameters. This emphasises the need for new experimental tests aimed at reducing these uncertainties.

In this work, we consider ice as an elastic, homogeneous isotropic material characterized by its Young's modulus E [MPa], its Poisson's ratio ν and its density ρ [g/cm^3]. These properties depend on the ice formation conditions: temperature, T [°C], Liquid Water Content, LWC [g/m^3], Median Volume Diameter, MVD [µm] and air velocity, V [m/s], and thus of the type of ice: rime (porous and opaque ice), glaze (dense and transparent ice) or mixed ice.

To simplify the representation of the ice type, we use the density ρ or the freezing fraction parameter denoted n_0, when the density is not available. The freezing fraction is a non-dimensional parameter that indicates the proportion of liquid water that freezes at the impact on a surface. Values of n_0 range from 0 (no freezing) to 1 (water freezes instantly) and provide an indication of the type of ice: values near 0.4 correspond to glaze ice, values near 1 correspond to rime ice, and intermediate values correspond to mixed ice.

Ice as a material is assumed to exhibit an elastic quasi-brittle behavior in traction, it deforms elastically before cracking once a critical stress σ_c [MPa] is reached in its bulk denoted as σ_c^{bulk}. At its interface with a substrate, the ice can reach a critical stress, denoted as σ_c^{int}, which characterizes the debonding of the ice from the interface.

The critical energy release rate G_c [mJ/mm^2] characterises the dissipated energy in [mJ] per unit crack growth area. It can be characterized in a normal mode (mode I) and two shear modes (modes II/III), both within the bulk material and at the interface, respectively denoted as G_c^{bulk} and G_c^{int}. Firstly, we have synthesised the *bulk* material data used in the phase-field model, particularly for the estimation of the internal length l_c using Eq. 10. Secondly, we have synthesised the *interface* material data used for the cohesive zone model.

A. Bulk material properties

The *bulk* mechanical properties have been identified according to different tests:

- The Brazilian test, originally developed for concrete, was conducted in *Study n°1* to measure the volumetric critical stress at failure of ice, σ_c^{bulk}.
- A compression test was conducted in *Study n°1* to measure the Young's modulus, E.
- The plane-strain fracture-energy (PSFE) test was conducted in *Study n°2*, inspired from [21], to determine by calculation the bulk critical energy release rate crack propagation in mode I, $G_{c,\text{I}}^{\text{bulk}}$.

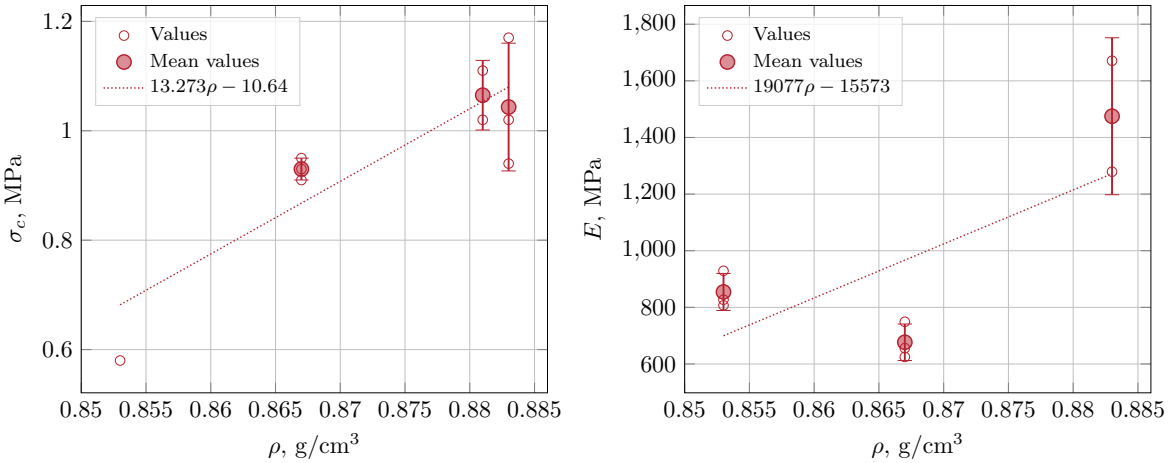

Fig. 7 σ_c^{bulk} **vs. density** ρ **(left) and Young's modulus** E **vs. density** ρ **(right)**

We can observe in Fig. 7 that it is difficult to determine a clear trend for these parameters as a function of density, particularly in the limited range of densities used here.

We have compiled the mean and standard deviation values for σ_c^{bulk} from Fig. 7 into Table 1, and for E into Table 2 with the lowest mean values highlighted in red and the highest in blue.

Table 1 σ_c^{bulk} **mean and standard deviation values according to** ρ **in** ***Study n°1***

ρ[g/cm^3]	σ_c^{bulk} mean [MPa]	σ_c^{bulk} std [MPa]
0.853	0.58	–
0.867	0.93	0.019
0.881	1.065	0.063
0.883	1.043	0.116

Table 2 E **mean and standard deviation values according to** ρ **in** ***Study n°1***

ρ[g/cm^3]	E mean [MPa]	E std [MPa]
0.853	854.3	65.43
0.867	676.6	64.53
0.883	1475.0	277.18

To calculate $G_{\text{c,I}}^{\text{bulk}}$, the PSFE test was conducted in *Study n°2*, as described in [22] for accreted ice. It is an experimental method that involves pressurizing a circular crack situated within the ice bulk until the specimen fractures at a critical pressure P_{c}, measured during the test. Then, the bulk critical energy release rate $G_{\text{c,I}}^{\text{bulk}}$ has been calculated as follow:

$$G_{\text{c,I}}^{\text{bulk}} = \frac{P_{\text{c}}^2 c}{E f\left(\frac{h}{c}\right)} \tag{11}$$

Where P_{c} [MPa] is the critical pressure measured at fracture, c [mm] is the radius of the circular crack, h [mm] the position of the circular crack within the ice bulk and $f\left(\frac{h}{c}\right)$ is a geometrical function defined for bulk fracture in [22]. The data of P_{c}, h and $f\left(\frac{h}{c}\right)$ have been synthesised in Table 3 for the circular crack radius c = 3mm.

Table 3 Measured and calculated parameters from the PSFE test for cohesive fracture in *Study n°2*

P_c[MPa]	h[mm]	$f\left(\frac{h}{c}\right)$	ρ[g/cm^3]
2.79	15	2.586	0.87
2.703	25	2.883	0.87
3.004	40	3.080	0.87
2.139	20	2.764	0.87
3.872	20	2.764	0.882
3.807	18	2.702	0.882
3.068	20	2.764	0.882
2.824	20	2.764	0.882
3.016	25	2.883	0.882
3.201	30	2.967	0.882
3.001	30	2.967	0.882
3.504	30	2.967	0.882
3.077	25	2.883	0.882
3.774	25	2.883	0.882
3.95	30	2.967	0.882

To calculate $G_{c,I}^{bulk}$ using Eq. 11, we also need a value for the Young's modulus E and because it was not calculated in the *Study n°2*, we use the one measured in the *Study n°1* and illustrated Fig. 7 (right). However, the Young's modulus obtained from *Study n°1* has not been measured for the same density values as in *Study n°2*. Therefore, we used a linear least squares regression on the Young's modulus E to estimate its values for density of *Study n°2*, $\rho \in \{0.87, 0.882\}$, as depicted in Fig. 7 (right) with the function $E(\rho) = 19077\rho - 15573$. Hence, we obtain the $G_{c,I}^{bulk}$ values represented on Fig. 8 and synthesised in terms of mean value and standard deviation in Table 4.

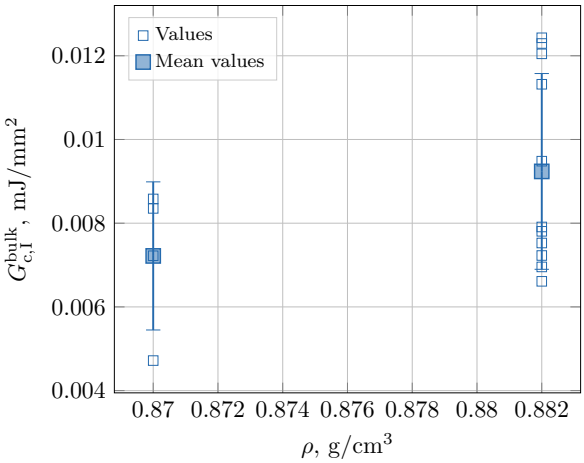

Fig. 8 Bulk critical energy release rate $G_{c,I}^{bulk}$ vs. density ρ

Table 4 $G_{c,I}^{bulk}$ mean and standard deviation values according to ρ in *Study n°1*

ρ[g/cm^3]	$G_{c,I}^{bulk}$ mean [mJ/mm^2]	$G_{c,I}^{bulk}$ std [mJ/mm^2]
0.87	0.0072	0.0017
0.882	0.0092	0.0023

The $G_{c,I}^{bulk}$ values shown in Fig. 8 illustrate the variability in the mechanical properties of ice for identical and for different ice formation conditions, reduced to the density parameter here.

Finally, The internal length l_c of the phase-field fracture model can be related to the ice properties using Eq. 10. Since the phase-field method is employed to describe volumetric fracture, we use the Young's modulus E, the volumetric critical stress σ_c^{bulk}, and the bulk critical energy release rate $G_{c,I}^{bulk}$, to calculate l_c as illustrated Fig. 9. Therefore, to maintain consistency of the calculated internal length in relation to the aforementioned mechanical parameters, we also employed a linear least squares regression on the bulk critical stress σ_c^{bulk} to estimate its values for density of *Study n°2*, $\rho \in \{0.87, 0.882\}$, as depicted Fig. 7 (left) with the function $\sigma_c^{bulk}(\rho) = 13.273\rho - 10.64$.

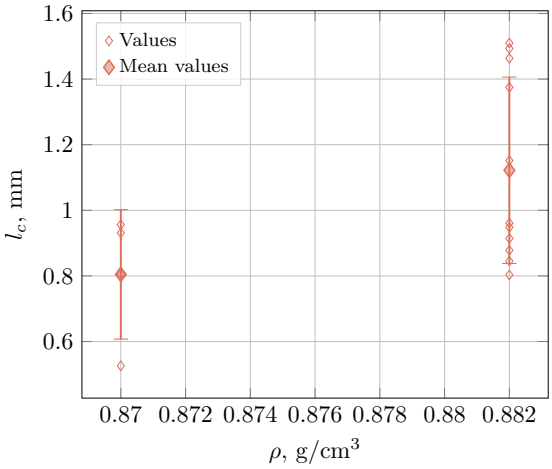

Fig. 9 Phase-field internal length values l_c for AT2 model calculated using Eq. 10

It can be observed that the variability in the mechanical properties of ice extends across the values of the internal length. The mean values are centered around $l_c = 1$mm as represented Fig. 9 and Table 5, which represents the "crack thickness" in the phase-field model.

Table 5 Calculated internal length values according to Eq. 10 with mean and standard deviation values

ρ	l_c mean [mm]	l_c std [mm]
0.87	0.804	0.197
0.882	1.122	0.284

B. Interface material properties

The *interface* mechanical properties have been identified according to different tests:

- The Crack Lap Shear (CLS) test was conducted in *Study n°1*, inspired from [23], to determine the interface critical energy release rate for crack propagation in mode II, $G_{c,II}^{int}$, between ice and one substrate studied.
- A shear test was developed in *Study n°2* to determine the interfacial critical stress of ice on different substrates σ_c^{int}.

The procedures for the CLS and shear tests are not detailed here. Instead, the values of $G_{c,II}^{int}$ and σ_c^{int} are shown respectively in Fig. 10 left and Fig. 10 right. For clarity, only the mean values of $G_{c,II}^{int}$ are presented. Additionally, due to a lack of density data for the shear test, the σ_c^{int} values are illustrated with respect to the freezing fraction n_0.

It is observed in Fig. 10 left and Table 6, that the interface critical energy release rate values in shear mode (mode II) are highly dispersed across a wider density range. Generally, the magnitude of $G_{c,II}^{int}$ is significantly higher than $G_{c,I}^{bulk}$. This could suggests a dependence on the type of fracture, whether cohesive or adhesive, with varying surface energy due to the difference between ice cohesion in the bulk and ice adhesion to a particular substrate. Additionally, the variation between failure modes, traction/normal mode (mode I) and shear mode (mode II), could indicate a dependence on the ice microstructure, as grain formation and growth can differ from one experiment to another for different ice formation conditions and create an anisotropic behaviour.

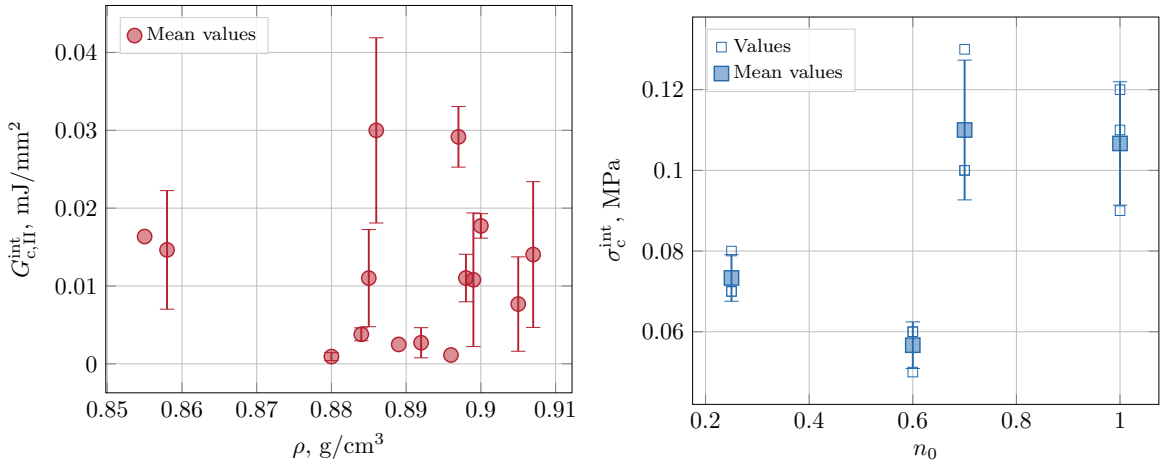

Fig. 10 Interface critical energy release rate $G_{c,II}^{int}$ vs. density ρ (left) and shear critical stress σ_c^{int} vs. density ρ

The shear stress σ_c^{int} shown in Fig. 10 (right) exhibits less, but still significant dispersion, with values nearly 10 times smaller in magnitude compared to the volumetric critical stress σ_c^{bulk}.

Similar to the interface critical energy release rate in mode II $G_{c,II}^{int}$, the critical shear stress appears to depend on the ice formation conditions, represented here by the freezing fraction. However, the critical shear stress shows a ratio of 2 between its maximum and minimum values.

Table 6 $G_{c,II}^{int}$ mean and standard deviation values according to ρ in *Study n°1*

ρ[g/cm^3]	$G_{c,II}^{int}$ mean [mJ/mm^2]	$G_{c,II}^{int}$ std [mJ/mm^2]
0.855	0.01635	–
0.858	0.01463	0.0076
0.88	0.00093	0.00051
0.884	0.00379	0.00083
0.885	0.01101	0.00624
0.886	0.02999	0.0119
0.889	0.00249	–
0.892	0.00270	0.0019
0.896	0.00113	–
0.897	0.02916	0.0039
0.898	0.01102	0.0030
0.899	0.0108	0.0086
0.9	0.01771	0.0016
0.905	0.00767	0.0061
0.907	0.01404	0.0094

To conclude this section, we have identified the different parameters required for the fracture models presented in sections III.A and III.B. The main findings indicate that the mechanical properties of ice exhibit significant variability due to its brittle nature and different formation conditions, simplified here to density and freezing fraction but also to the assumptions made regarding the range of Young's modulus for the calculation of bulk critical energy release rate in mode I. In addition, uncertainties may arise from the different experimental procedures used in *Study n°1* and *Study n°2*, highlighting the need for new experimental tests aimed at reducing these uncertainties.

Given the scattered nature of the data, we have selected the model parameters, while close in magnitude to the actual values, to understand the relationships between them in terms of "numerical behaviour" rather than to accurately

Table 7 σ_c^{int} mean and standard deviation values according to n_0 in *Study n°1*

n_0	σ_c^{int} mean [MPa]	σ_c^{int} std [MPa]
0.2	0.073	0.0058
0.6	0.057	0.0058
0.7	0.11	0.0173
1.0	0.106	0.0153

represent the physical properties of the ice material. Therefore, in the Section V, we relate the phase-field parameter G_c^{pf} to $G_{c,I}^{bulk}$, as listed in the Table 8, and the cohesive zone parameters G_c^{czm} to $G_{c,II}^{int}$ and σ_c^{czm} to σ_c^{int} as listed in Table 10.

V. Results

The purpose of this section is to highlight the benefits of the proposed numerical strategy as well as its current limitations through qualitative analyses.

As explained in the previous section, the physical properties of the ice and the interface are currently difficult to estimate. This is mainly due to the large scattering of data due to i) the intrinsic materiel dispersion, ii) the lack of consistency of the whole test campaigns and iii) the difficulty to link the mechanical properties to the accretion parameters. For convenience, and especially to handle reasonable internal length l_c with regards to the mesh used in this study, we may therefore use material data that are slightly different from the one exhibited in section IV (same order of magnitude but sometime at the tail of the distrbution).

We present here two sets of results related to the test case illustrated in Fig 2. The purpose of Section V.A is to study the way one effectively control the energy dissipated by the fracture phase-field model independently from the cohesive zone model. In particular we are interested in testing two ice/subtrate insterface meshing strategies. Section V.A therefore deals with a finely discretised two-dimensional (under plane strain assumption) model without cohesive zone model. In section V.B we take into account some of the conclusions of the first study and one focuses on a three-dimensional problem that includes both phase-field fracture and cohesive zone models as detailed in section III. We give further insights on the origin of the multi-fracture pattern and we study the influence of the "weak" or "strong" character of the interface.

A. Two-dimensional case with phase-field model only

We focus here on a two-dimensional version of the problem presented in Fig. 2 modeled under the plane strain assumption (thickness is $t = 1$ mm). The problem is modeled in a non-rotating reference frame and a centrifugal volume force $\rho r\Omega^2 \vec{e}_r$ is applied to the whole volume according to the angular velocity rate $\dot{\Omega} = 830\text{rad/s}^2$. The $r = 0$mm face of the aluminum substrate is clamped while the $r = 0$mm face of the ice is free (see Fig. 2). The material properties of the ice and alumina used in this model are given in Table 8. The differences in density and Young's modulus tends to generate a bending of the whole structure.

Table 8 Material properties of the 2D model

Property	Ice	Aluminum
E [MPa]	1500	69000
ν	0.31	0.325
ρ [g/cm^3]	0.917	2.7
G_c^{bulk} [mJ/mm^2]	10^{-3}	–
σ_c^{bulk} [MPa]	0.4	–
l_c [mm] (calculated from Eq. 10)	1.0	–

As stated in introduction and in section III.C, the calculation is performed with Z-set in implicit dynamics with an α-method integration scheme. As explained earlier, the staggered scheme requires to solve alternately two finite element problems. In the case where no cohesive model is used, the discretisation strategy of the mechanical problem

necessitates the continuity of the displacement at the interface and the "attached node" strategy is used (see Fig. 11). However one has the choice for the phase-field problem to "attach" or "detach" nodes. If the attached nodes strategy is used, then one needs to use very high values for G_c^{pf} and σ_c^{pf} for the aluminum to prevent damage in the substrate. In the case of the detached nodes strategy, a fictitious interface appears in the phase-field problem and the boundary condition (5b) naturally applies.

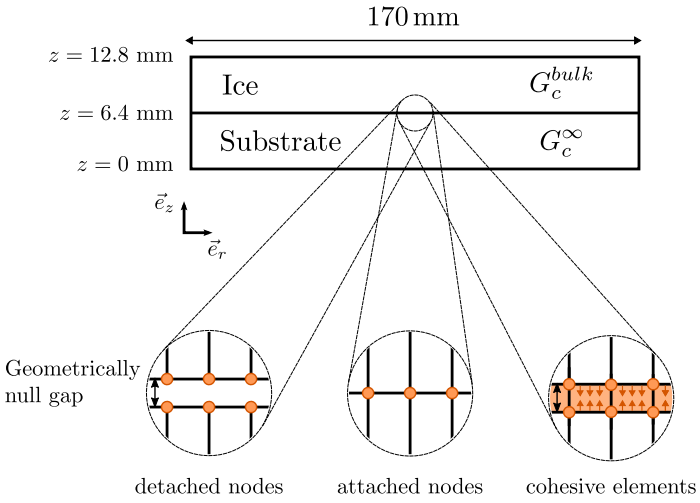

Fig. 11 Differents interface meshing strategies.

The phase field ϕ computed for the two meshing strategies are depicted in Fig. 12 at final failure. The failure sequence is similar for the 3D case and will be discussed in section V.B, but one can notice in both cases the appearance of a pattern of vertical (transverse) cracks linked by a horizontal bulk crack very close to the interface.

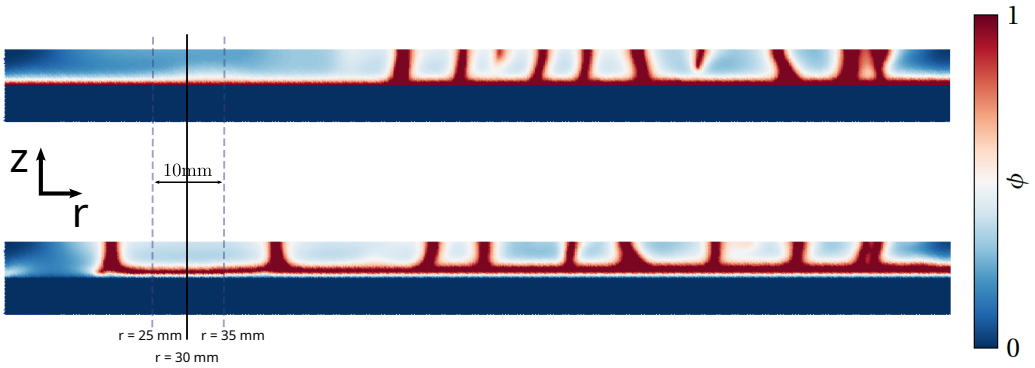

Fig. 12 Result of phase-field nodal variable ϕ for detached nodes (top) and attached nodes (bottom)

The vertical profile of ϕ at $r = 30$ mm for the two meshing strategies are plotted in Fig. 13 (note that the $r = 30$ mm position is identified in Fig. 12). It can be observed that the localization of cracks (when $\phi = 1$) varies depending on the meshing strategy. When the mesh is detached, the crack is located exactly at the interface, forming a half-cut profile, whereas when the mesh is attached, the crack is located slightly before the interface. In this latter situation, the very high G_c on the aluminum side penalises the growth of ϕ at the interfacial node and the value remains very close to 0. The crack "center" ($\phi = 1$) is therefore located slightly away from the interface. For detached nodes, the boundary condition $\vec{\nabla}\phi.\vec{n} = 0$ leads to a flat spot on the curve very close to the interface. In both cases, $\phi > 0$ at the upper surface of the sample. This is because the AT2 model is known to exhibit damage as soon as the loading is not null (there is no damage threshold) and also because the overall centrifugal loading constantly keeps applying traction everywhere. A model exhibiting a threshold like the AT1 [9] one could limit this phenomena but it is out of the scope of this study.

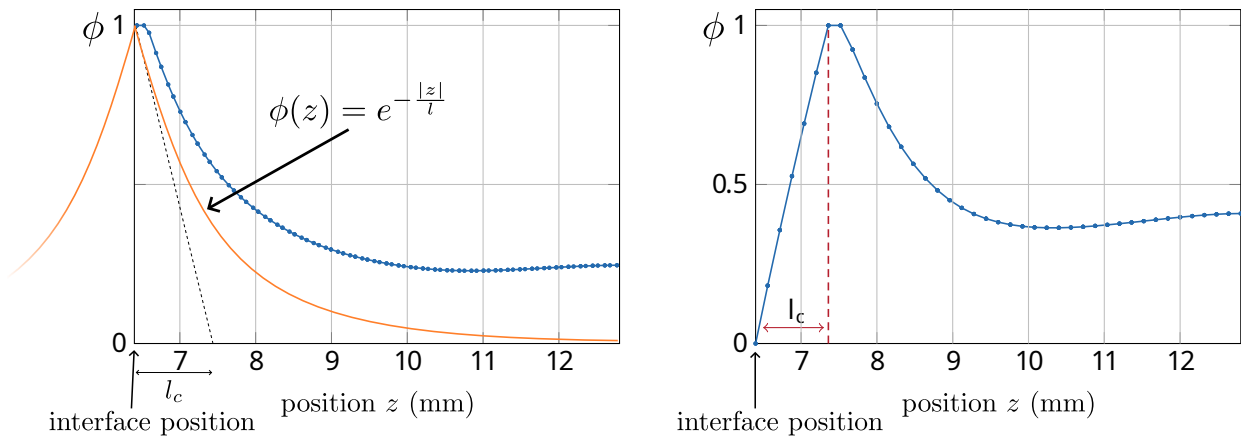

Fig. 13 Cross-sectional nodal damage profile $\phi(z)$ in the ice at $r = 30$ mm (in blue) for detached mesh (left) and attached mesh (right). The orange line represents the theorical profile of ϕ for a perfect crack loaded at infinity in a one-dimensional problem (see [14]).

We now look at the energy dissipated during the fracture process for both cases. In a general way, we can use expression of Ψ_c (Eq. 2) to compute the energy dissipated during the cracking process. Because the crack pattern is complex at the end of the simulations, one can restrict the analysis to a relatively simple zone. The area delimitated by $r \in [25\text{mm}, 35\text{mm}]$ exhibits on both simulation a single longitudinal crack of length $L_{\text{crack}} = 10\text{mm}$ whithout any branching. The numerical evaluation of Ψ_c through expression (2) is therefore performed over the restricted domain $r \in [25\text{mm}, 35\text{mm}] \times z \in [6.4\text{mm}, 12.8\text{mm}]$. Results are presented in Table 9. G_c^{bulk} is the parameter set up in the simulations and a perfect brittle crack of length L_{crack} and thickness $t = 1$ mm would have dissipated 0.01 mJ. $E_{\text{diss}}^{\text{det.}}$ and $E_{\text{diss}}^{\text{att.}}$ are the energies dissipated respectively for the "detached nodes" and the "attached nodes" strategy.

For the detached nodes strategy, the dissipated energy is about 73% of the expected one. This can be explained invoking two reasons. The first one is that the interfacial boundary condition generates a "half-cut" profile. A perfect crack in a infinite unidimensional media modeled with a phase-field would lead to the orange profile of Fig. 13 at both side of the crack center (see [14] for details). According to the phase-field theory, the associated dissipation tends to G_c when $l_c \to 0$. This perfect crack is far from being the one studied here, but one could expect decrease of about 50% of the theorical dissipation because of this half-profile. On the other hand, due to structural effects and the fact that the AT2 model does not include a damage threshold, the damage nevers drops to 0 away from the crack center which compensate in some way the previous decrease leading to a value of dissipated energy of 0.0073 mJ. The control of the dissipated energy is therefore not perfect. A possible way of improving this control could be the introduction of an anisotropic toughness as proposed in [24] or [25] which would allow to dissipate more energy for cracks propagating in the $\vec{e}_r$ direction and thus submitted to interactions with the interface. The joint use of damage threshold models such as the AT1 [9] would also be an interesting approach.

For the attached nodes strategy, the dissipated energy is much closer to the theorical one. This similarity is however suspicious since like in the previous case, ϕ does not drop to 0 far from the crack center. But the real problem with this strategy is that due to the high aluminum G_c, the phase-field is close to 0 at the interface, which would lead to a cut-off of the interactions by stress concentration with a possible cohesive zone model.

For this reason, the "detached nodes" strategy is retained to mesh the phase field problem for the following three-dimensional case which includes a cohesive zone model.

Table 9 Results of dissipated energy for: perfect crack, "detached nodes," and "attached nodes" cases

G_c^{pf} [mJ/mm^2]	$G_c^{\text{pf}} \times L_{\text{crack}} \times t$ [mJ]	$E_{\text{diss}}^{\text{det.}}$ [mJ]	$E_{\text{diss}}^{\text{att.}}$ [mJ]
0.001	0.010	0.0073	0.0097

B. Three-dimensional case with phase-field model coupled with cohesive zone model

This section is devoted to assess the joint phase-field / cohesive zone approach. We use the same geometry as the one illustrated in Fig 2 with a three-dimensional finite element model. Three cases are treated for different interface properties of the cohesive zone model (Table 10): "strong" interface where the volume and interface parameters G_c^{czm} and σ_c^{czm} are similar, 'weak' interface where the interface parameters G_c^{czm} and σ_c^{czm} are respectively divided by 4 and 2 respectively and an "intermediate" case between the two previous ones. These cases are proposed to investigate how the substrate's properties influence its interaction with the ice at the interface and with the phase-field model in its bulk. In all three cases, the internal length of the phase-field model is fixed to l_c = 1 mm and the mesh size to h = 1.7 mm.

Table 10 Different cases based on interface properties

		Strong interface	Intermediate interface	Weak interface
$G_{\mathrm{c}}^{\mathrm{czm}}$	mJ/mm^2	0.001	0.00056	0.00025
$\sigma_{\mathrm{c}}^{\mathrm{czm}}$	MPa	0.4	0.3	0.2
$G_{\mathrm{c}}^{\mathrm{pf}}$	mJ/mm^2	0.001	0.001	0.001
$\sigma_{\mathrm{c}}^{\mathrm{pf}}$	MPa	0.4	0.4	0.4
l_{c}	mm	1.0	1.0	1.0

In the case of an "intermediate" interface, effective interaction between the phase-field and cohesive zone models is observed (Fig. 14). Firstly, as shown at frame 2 in Fig. 16, at t = 0.5256s a crack initiates in the ice bulk close to the center of rotation. This is explain by th fact that the radial stress σ_{rr}, reaches the critical stress $\sigma_c^{\mathrm{pf}} \approx 0.4$ MPa. It is shown in the blue curve Fig. 15 (top left) where the radial stress is extracted at z = 12.8mm.

Then, a shear stress wave propagates in a dynamic regime near the interface resulting in a damage propagation in the ice bulk near-interface (frame 3 to 6 in Fig. 16). At the position $r \approx$ 110mm, the shear stress σ_{rz} reaches the critical value σ_c^{czm} = 0.3MPa (red curve in Fig. 15 bottom left). This is the point at which the phase-field damage variable near the interface ceases to evolve, and the cohesive zone elements at the interface begin to experience damage (around frame 7 in Fig. 16).

Finally, as the shear wave propagates and reaches the end of the bar (frame 12 in Fig. 16), we observe stress waves reflecting back in the bulk. These phenomena appear to induce additional fractures within the bulk of the ice, resulting in a multi-fracture pattern observed from frame 13 to 20 Fig. 16.

Remarks:

- In frame 1 of Fig. 16, damage initiation is observed within the cohesive zone at r = 0 mm due to stress concentration. However, this damage does not propagate further.
- It can be observed that during the propagation of the shear wave, the radial stress shifts into compression, indicated by negative values of σ_{rr} (as shown by the blue curve in Fig. 15, bottom). However, the compressive stress does not affect the fracture process since the source term Ψ_0^+ in the phase-field equation exclusively addresses traction solicitations via the positive part decomposition introduced in Eq. 6.

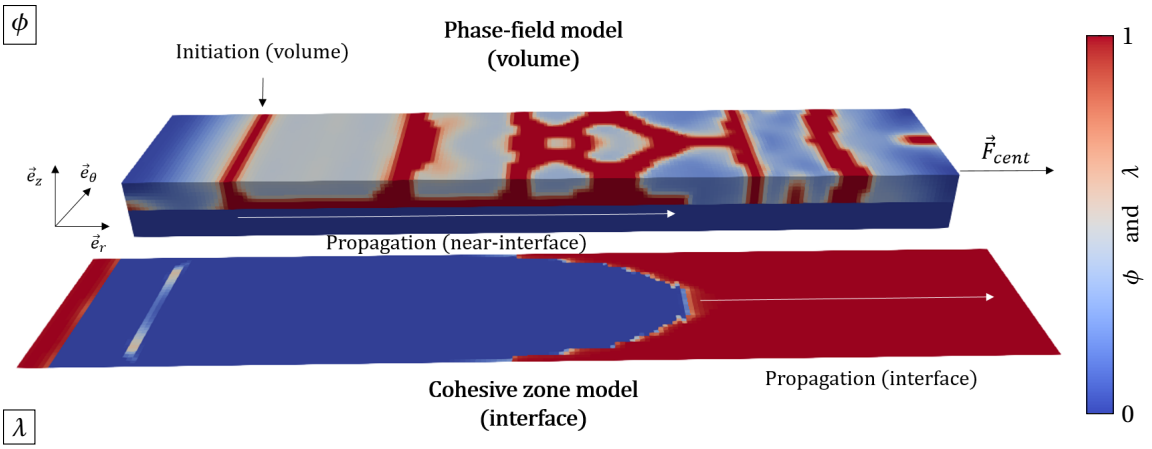

Fig. 14 The "intermediate" case results for the damage variables of the phase-field model in the volume (top) and cohesive zone model at the interface (bottom) without the displacement solution

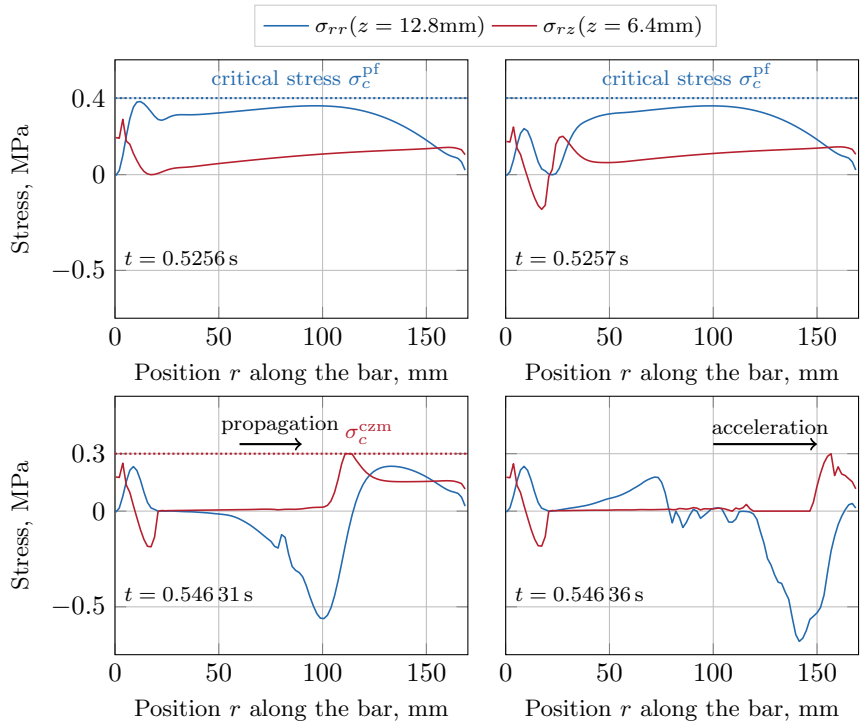

Fig. 15 Evolution of the radial stress σ_{rr} (blue) in the ice bulk (height $z = 12.8$mm) and shear stress σ_{rz} (red) and the propagation of the shear wave at interface (height $z = 6.4$mm) for different simulation times.

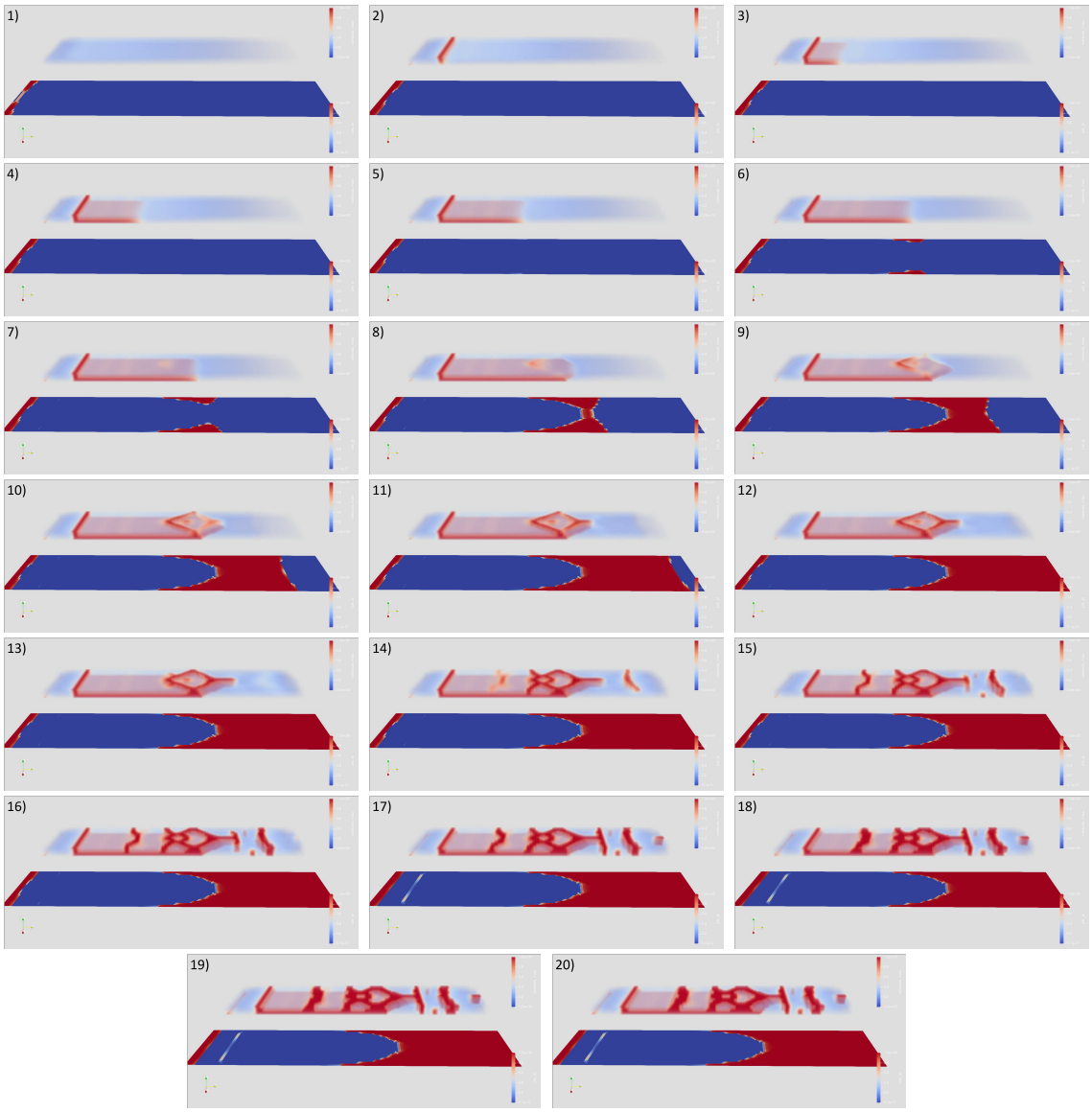

Fig. 16 The complete evolution (reduced to 20 frames) of the damage variables in phase-field and cohesive zone models for the "intermediate" case (Transparency has been introduced into the ice bulk to enhance the visibility of the damage variable ϕ)

In the same stress analysis, for the case involving a "strong" interface, we observe crack initiation within the bulk and its propagation along the near-interface, driven by shear wave propagation. However, the critical stress of the cohesive zone model, $\sigma_c^{\text{czm}} = 0.4$MPa, is never reached, preventing damage at the interface (Fig. 17 bottom).

Conversely, in the case of the "weak" interface, a crack initiates at the interface at the center of rotation due to stress concentration at $r = 0$mm. The crack then propagates along the interface via a shear wave. Upon reaching the end of the bar, it generates a multi-fracture pattern in the bulk (refer to Fig. 17 top) as a result of wave reflections.

In all three cases, multiple fracture patterns are observed and potentially identifiable as ice debris as illustrated for the "strong" case depicted in Fig. 18 when the damage is shown in the deformed configuration.

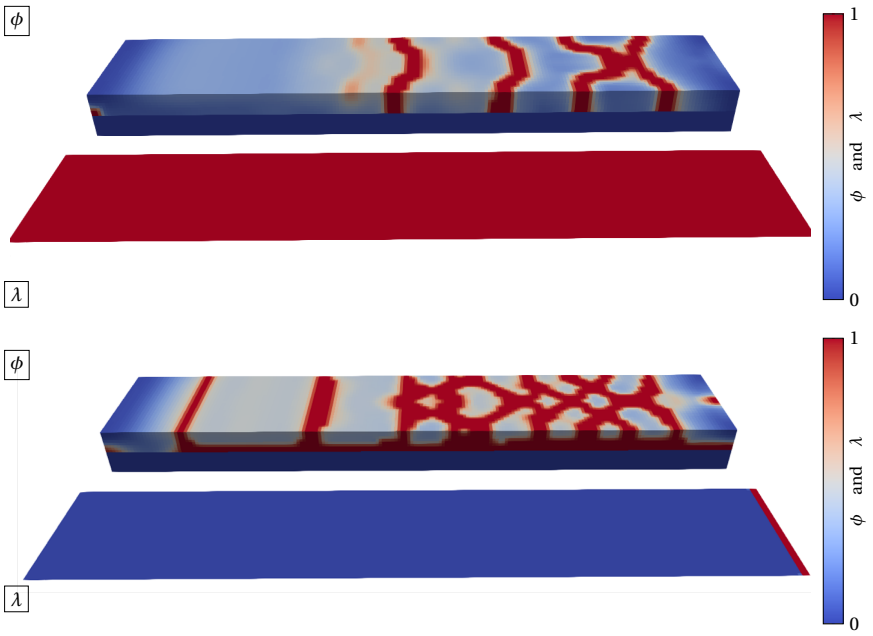

Fig. 17 The "weak" case (top) and the "strong" case (bottom) with phase-field and cohesive zone variables without the displacement solution

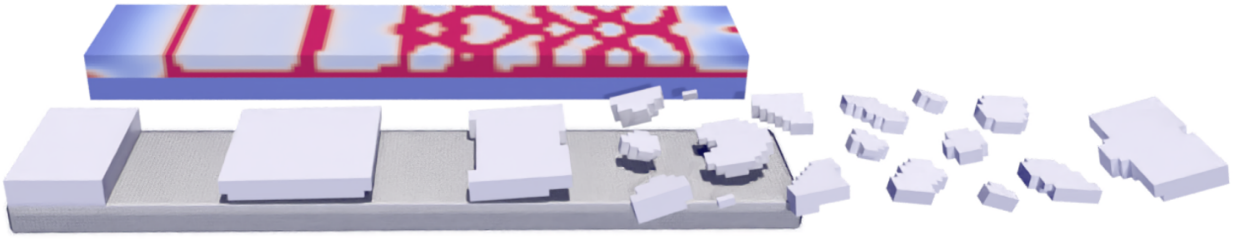

Fig. 18 The "strong" interface case with the phase-field solution (top) and the displacement solution (bottom)

VI. Conclusion

In this work, a methodology to model ice shedding from rotating parts is presented in a 3D finite element framework. The mechanisms leading to ice shedding are described using a coupling between phase-field fracture and cohesive zone models that provide insights into the mechanical behavior of ice when breaking under centrifugal loading. To understand the possible cracks interactions between the phase-field and cohesive zone models, we investigate three cases for different interface properties, categorizing them into "strong", "intermediate" and "weak" cases based on parameters G_c^{czm}, σ_c^{czm}.

The simulation revealed distinct responses, under centrifugal loading, on the initiation and propagation of cracks in both the volume and interface. In both "strong" and "intermediate" cases, we observe a crack initiation within the volume, due to radial stresses and a transition to the near-interface, with the phase-field model, in the "strong case" Fig. 10 down) or a transition to the near-interface and then at the interface, with the cohesive elements, in the "intermediate" case (Fig. 8) following a shear stress wave.

Further investigations will explore crack nucleation within the bulk material both during and after propagation. This research encompasses studying the dynamics of wave propagation, including acceleration of a crack speed with a deceleration at the onset of new crack formation within the ice volume, a phenomenon known as branching, detailed in [26]. Additionally, the research will focus on crack nucleation that occurs immediately after stress wave reflections, specifically examining stress analysis under multi-axial conditions involving radial and shear stresses, as discussed in [27]. Comparing numerical results to the real experiment of Fig 2 is also an ongoing work.

In addition, this study highlights the importance of the mechanical properties of ice in understanding its behaviour under different formation conditions. Through rigorous examination of parameters such as Young's modulus, critical stresses and critical energy release rate at the bulk and interface, we acquire essential insights into how ice reacts to mechanical stresses induced in particular by centrifugal loading. These properties play an important role in forecasting phenomena such as crack initiation and propagation. Continued advancements in characterizing ice's mechanical behavior through consistent mechanical experiments will further enhance our understanding of its behavior.

This research contributes to the broader understanding of ice shedding phenomena in rotating systems, particularly in the context of material mechanical properties, associated with phase-field and cohesive zone models. Future work may delve into additional complexities, refine modeling parameters, and explore real-world applications to further enhance the predictive capabilities of the presented methodology with 3D industrials applications of aircraft engine fan blade.

References

[1] Francfort, G., and Marigo, J.-J., "Revisiting brittle fracture as an energy minimization problem," *Journal of the Mechanics and Physics of Solids*, Vol. 46, No. 8, 1998, pp. 1319–1342. https://doi.org/10.1016/S0022-5096(98)00034-9, URL https://linkinghub.elsevier.com/retrieve/pii/S0022509698000349.

[2] Bourdin, B., Francfort, G., and Marigo, J.-J., "Numerical experiments in revisited brittle fracture," *Journal of the Mechanics and Physics of Solids*, Vol. 48, No. 4, 2000, pp. 797–826. https://doi.org/10.1016/S0022-5096(99)00028-9, URL https://linkinghub.elsevier.com/retrieve/pii/S0022509699000289.

[3] Dugdale, D., "Yielding of steel sheets containing slits," *Journal of the Mechanics and Physics of Solids*, Vol. 8, No. 2, 1960, pp. 100–104. https://doi.org/10.1016/0022-5096(60)90013-2, URL https://linkinghub.elsevier.com/retrieve/pii/0022509660900132.

[4] Barenblatt, G., "The Mathematical Theory of Equilibrium Cracks in Brittle Fracture," Elsevier, 1962, pp. 55–129. https://doi.org/https://doi.org/10.1016/S0065-2156(08)70121-2, URL https://www.sciencedirect.com/science/article/pii/S0065215608701212.

[5] Bennani, L., Villedieu, P., Salaun, M., and Trontin, P., "Numerical simulation and modeling of ice shedding: Process initiation," *Computers & Structures*, Vol. 142, 2014, pp. 15–27. https://doi.org/10.1016/j.compstruc.2014.06.001, URL https://linkinghub.elsevier.com/retrieve/pii/S0045794914001333.

[6] Bennani, L., Villedieu, P., and Salaun, M., "A mixed adhesion–brittle fracture model and its application to the numerical study of ice shedding mechanisms," *Engineering Fracture Mechanics*, Vol. 158, 2016, pp. 59–80. https://doi.org/10.1016/j.engfracmech.2016.02.050, URL https://linkinghub.elsevier.com/retrieve/pii/S0013794416300765.

[7] Marbœuf, A., Bennani, L., Budinger, M., and Pommier-Budinger, V., "Electromechanical resonant ice protection systems: numerical investigation through a phase-field mixed adhesive/brittle fracture model," *Engineering Fracture Mechanics*, Vol. 230, 2020, p. 106926. https://doi.org/https://doi.org/10.1016/j.engfracmech.2020.106926, URL https://www.sciencedirect.com/science/article/pii/S0013794419311014.

[8] "ICE GENESIS Project Overview," , 2019. URL https://www.ice-genesis.eu/.

[9] Pham, K., Amor, H., Marigo, J.-J., and Maurini, C., "Gradient Damage Models and Their Use to Approximate Brittle Fracture," *International Journal of Damage Mechanics*, Vol. 20, No. 4, 2011, pp. 618–652. https://doi.org/10.1177/1056789510386852, URL http://journals.sagepub.com/doi/10.1177/1056789510386852.

[10] Griffith, A. A., and Taylor, G. I., "VI. The phenomena of rupture and flow in solids," *Philosophical Transactions of the Royal Society of London. Series A, Containing Papers of a Mathematical or Physical Character*, Vol. 221, No. 582-593, 1921, pp. 163–198. https://doi.org/10.1098/rsta.1921.0006, URL https://royalsocietypublishing.org/doi/abs/10.1098/rsta.1921.0006.

[11] Rannou, J., and Bovet, C., "Domain decomposition methods and acceleration techniques for the phase field fracture staggered solver," *International Journal for Numerical Methods in Engineering*, 2024, p. e7544. https://doi.org/https://doi.org/10.1002/nme.7544, URL https://onlinelibrary.wiley.com/doi/abs/10.1002/nme.7544.

[12] Wu, J.-Y., Nguyen, V. P., Thanh Nguyen, C., Sutula, D., Bordas, S., and Sinaie, S., "Phase field modelling of fracture," *Advances in Applied Mechanics*, Vol. 53, 2019, pp. 1–183, https://www.sciencedirect.com/science/article/pii/S0065215619300134.

[13] Fortin, G., Beisswenger, A., and Perron, J., "Centrifuge Adhesion Test to Evaluate Icephobic Coatings," *AIAA Atmospheric and Space Environments Conference*, American Institute of Aeronautics and Astronautics, Toronto, Ontario, Canada, 2010. https://doi.org/10.2514/6.2010-7837, URL https://arc.aiaa.org/doi/10.2514/6.2010-7837.

[14] Miehe, C., Hofacker, M., and Welschinger, F., "A phase field model for rate-independent crack propagation: Robust algorithmic implementation based on operator splits," *Computer Methods in Applied Mechanics and Engineering*, Vol. 199, No. 45-48, 2010, pp. 2765–2778. https://doi.org/10.1016/j.cma.2010.04.011, URL https://linkinghub.elsevier.com/retrieve/pii/S0045782510001283.

[15] Borden, M. J., Verhoosel, C. V., Scott, M. A., Hughes, T. J., and Landis, C. M., "A phase-field description of dynamic brittle fracture," *Computer Methods in Applied Mechanics and Engineering*, Vol. 217, 2012, pp. 77–95.

[16] Tanné, E., Li, T., Bourdin, B., Marigo, J.-J., and Maurini, C., "Crack nucleation in variational phase-field models of brittle fracture," *Journal of the Mechanics and Physics of Solids*, Vol. 110, 2018, pp. 80 – 99. https://doi.org/https://doi.org/10.1016/j.jmps.2017.09.006, URL http://www.sciencedirect.com/science/article/pii/S0022509617306543.

[17] Turon, A., Dávila, C., Camanho, P., and Costa, J., "An engineering solution for mesh size effects in the simulation of delamination using cohesive zone models," *Engineering Fracture Mechanics*, Vol. 74, No. 10, 2007, pp. 1665–1682. https://doi.org/10.1016/j.engfracmech.2006.08.025, URL https://linkinghub.elsevier.com/retrieve/pii/S0013794406003808.

[18] Schellekens, J., and De Borst, R., "On the numerical integration of interface elements," *International Journal for Numerical Methods in Engineering*, Vol. 36, No. 1, 1993, pp. 43–66.

[19] Benzeggagh, M., and Kenane, M., "Measurement of mixed-mode delamination fracture toughness of unidirectional glass/epoxy composites with mixed-mode bending apparatus," *Composites Science and Technology*, Vol. 56, No. 4, 1996, pp. 439–449.

[20] "Z-set, material and structure analysis suite," , 2024. URL http://www.zset-software.com.

[21] Andrews, E. H., and Lockington, N. A., "The cohesive and adhesive strength of ice," *Journal of Materials Science*, Vol. 18, No. 5, 1983, pp. 1455–1465. https://doi.org/10.1007/BF01111965, URL https://doi.org/10.1007/BF01111965.

[22] Pervier, M. A., and Hammond, D. W., "Measurement of the fracture energy in mode I of atmospheric ice accreted on different materials using a blister test," Vol. 214, 2023, pp. 223–232. https://doi.org/10.1016/j.engfracmech.2019.02.003, URL https://www.sciencedirect.com/science/article/pii/S0013794418307641.

[23] Lai, Y.-H., Dwayne Rakestraw, M., and Dillard, D. A., "The cracked lap shear specimen revisited—a closed form solution," *International Journal of Solids and Structures*, Vol. 33, No. 12, 1996, pp. 1725–1743. https://doi.org/https://doi.org/10.1016/0020-7683(95)00124-7, URL https://www.sciencedirect.com/science/article/pii/0020768395001247.

[24] Bleyer, J., and Alessi, R., "Phase-field modeling of anisotropic brittle fracture including several damage mechanisms," *Computer Methods in Applied Mechanics and Engineering*, Vol. 336, 2018, pp. 213–236. https://doi.org/https://doi.org/10.1016/j.cma.2018.03.012, URL https://www.sciencedirect.com/science/article/pii/S0045782518301373.

[25] Karoui, Z., "Variational approaches to fracture for the modelling of matrix-cracking phenomena in unidirectional composite laminates," Ph.D. thesis, Sorbonne université / ONERA, 2023. URL https://theses.fr/2023SORUS043.

[26] Bleyer, J., Roux-Langlois, C., and Molinari, J.-F., "Dynamic crack propagation with a variational phase-field model: limiting speed, crack branching and velocity-toughening mechanisms," *International Journal of Fracture*, Vol. 204, No. 1, 2017, pp. 22. 79–100. https://doi.org/https://doi.org/10.1007/s10704-016-0163-1, URL http://infoscience.epfl.ch/record/222801.

[27] de Lorenzis, L., and Maurini, C., "Nucleation under multi-axial loading in variational phase-field models of brittle fracture," *International Journal of Fracture*, 2021. URL https://hal.science/hal-03224892.